C. R. Mecanique 340 (2012) 81–94

Contents lists available at SciVerse ScienceDirect

Comptes Rendus Mecanique

www.sciencedirect.com

Biomimetic flow control

Biomimetic bluff body drag reduction by self-adaptive porous flaps

Nicolas Mazellier *, Audrey Feuvrier, Azeddine Kourta

Laboratoire PRISME, Université d'Orléans, 8 rue Léonard de Vinci, 45072 Orléans cedex 2, France

ARTICLE INFO

Article history:
Available online 30 December 2011

Keywords:
Aerodynamics
Drag reduction
Flow separation
Passive control
Biomimetism

ABSTRACT

The performances of an original passive control system based on a biomimetic approach are assessed by investigating the flow over a bluff body. This control device consists of a couple of flaps made from the combination of a rigid plastic skeleton coated with a porous fabric mimicking the shaft and the vane of the bird's feathers, respectively. The sides of a square cylinder have been fitted with this system so that each flap can freely rotate around its leading edge. This feature allows the movable flaps to self-adapt to the flow conditions. Comparing both the uncontrolled and the controlled flow, a significant drag reduction ($\approx 22\%$ on average) has been obtained over a broad range of Reynolds numbers. This improvement is related to the increase of the base pressure in the controlled case. The investigation of the mean flow reveals a noticeable modification of the flow topology at large scale in the vicinity of the controlled cylinder. Meanwhile, the study of the relative motion of both flaps highlights that their dynamics is sensitive to the Reynolds number. Furthermore, the analysis of the flow dynamics at large scale suggests a lock-in coupling between the flap motion and the vortex shedding.

1. Introduction

The flow over a bluff body is a situation encountered in numerous engineering applications such as the aerodynamics of road vehicles or buildings undergoing wind loading. One of main features of bluff body flows relies on the onset of flow separation arising from either curvature or adverse pressure gradient effects. In most cases, flow separation is responsible for the alteration of the aerodynamic performances (e.g. drag increase) or structural vibrations (e.g. galloping), inducing consequently energy consumption excess and/or structural fatigue. Even though a large number of studies have been devoted to flow separation, it remains one of the most challenging issues of modern fluid dynamics.

In this context, flow control appears as one of the most attractive ways to prevent flow separation, or at least attenuate its effects. At first glance, one can distinguish between two main classes of control strategies: passive and active [1,2]. Unlike active control, passive control does not require external power supply. Intense efforts have been dedicated to the control of the flow around bluff bodies as evidenced by the abundant literature on this topic (see e.g. [2] and references therein). Here, we do not attempt to review the various flow control strategies and accordingly we only focus on drag reduction by means of passive control which mainly consists in shape modification. One can cite, for instance, the work performed by Bearman and Owen [3] who achieved up to 50% drag reduction of rectangular cylinders by introducing spanwise waviness of the front face. These authors pointed out that the vortex shedding was suppressed for an optimal wavelength, while the separated shear layer instabilities were still observed. Owen et al. [4] implemented protuberances at the surface of a circular cylinder following a helical pattern. This passive system enabled 25% drag reduction over one decade of Reynolds numbers. Recently, Shao and Wei [5] investigated the modification of the flow around a square cylinder at high Reynolds number

* Corresponding author.
E-mail address: nicolas.mazellier@univ-orleans.fr (N. Mazellier).

1631-0721/$ – see front matter
doi:10.1016/j.crme.2011.11.006

Fig. 1. Photography of a condor during the landing approach.

by means of a control rod. By displacing the control rod, the authors identified the location zones where the control was efficient. Their results indicated that the maximum drag reduction ($\approx 25\%$) was achieved when the control rod was located in the separated shear layers. In that configuration, the vortex shedding was almost annihilated. Bruneau and Mortazavi [6] simulated a porous layer around a square cylinder by means of a numerical penalization method over a broad range of Reynolds number. They pointed out that the wake topology was strongly sensitive to the porosity of the intermediate layer and reported up to 30% drag reduction. Even though these examples, chosen among others, suggest that passive control can lead to significant improvements, it turns out that the efficiency of this control strategy is often restricted to limited configurations. For instance, the results in Ref. [5] evidenced that the control efficiency was strongly dependent on both the Reynolds number and the shape of the controlling rod.

To overcome this drawback, the control system needs to self-adapt to the flow conditions. This is well demonstrated by aircraft for which the requirements vary during the flight (i.e. taking-off, cruising and landing phases) [7]. Biological observations of insects, birds, fishes and plants emphasized the ability of nature to develop efficient self-adaptive control systems [8–13]. These observations led to the concept of biomimetic flow control which gave rise to the design of numerous control devices (see [14,15] and references therein). One of the most famous examples of such devices is the ribbed surface inspired from shark's skin which has been used successfully to decrease wall shear stress [14]. Alben et al. [16] and then after Gosselin et al. [12] reported huge drag reduction induced by shape reconfiguration of flexible bodies set in a stream. Recently, Favier et al. [17] simulated the flow over a circular cylinder coated with movable cilia at low Reynolds number. The interplay between the coating and the large scale structure in the wake implied up to 15% drag reduction. The authors observed a lock-in phenomenon of the coating motion at a frequency slightly smaller than the natural (i.e. without cilia) vortex shedding frequency. Gosselin and de Langre [18] reported an experimental investigation of the aerodynamics of a sphere fitted with a poroelastic coating. Their results showed a significant drag reduction due to the reconfiguration of the hairy surface.

For high angles of attack, such as those experienced during landing, one can observe that a part of the plumage located on the upper side of bird's wings pops up (see Fig. 1). Liebe [19] interpreted this phenomenon as a consequence of the reverse flow induced by a flow separation enabling light feathers to depart from the wing surface. He assimilated this behavior to a lift enhancement system. Following the work of Liebe [19], Bechert et al. [14] mimicked a bird's feather by implementing a movable flap on the upper surface of an airfoil. During their experiments, this flap was activated by the flow separation arising at high enough angle of attack. Their results showed that this self-adaptive passive device was enable to delay stall. These authors suggested that the effective angle of attack is decreased when the feathers are activated and accordingly that the flow separation is delayed. This phenomenon was recently confirmed by Schatz et al. [20] who performed numerical simulations implementing comparable movable flap.

In this study, we develop and evaluate the performances of an original self-adaptive passive control device based on the works reported by Liebe [19], Bechert et al. [14] and Schatz et al. [20]. Our system consists of a couple of porous flaps designed to mimic the main features of bird's feathers. This control system is fitted on the sides of a square cylinder model which is well documented in literature. The experimental set-up allows the control flaps to freely rotate around their leading edge. This system is therefore activated by the flow separation arising at the corners of the square cylinder [21]. The work reported here is dedicated to the investigation of the control system dynamics and its interplay with the flow. A specific attention is paid to the aerodynamic performances of the controlled square cylinder.

The article is organized as follows. The experimental set-up and the measurement techniques are detailed in Section 2. The main features of the uncontrolled flow are described in Section 3 and will provide a reference case. Then, the design of the original control system developed in this study is introduced in Section 4. A particular focus is given to the dynamics of

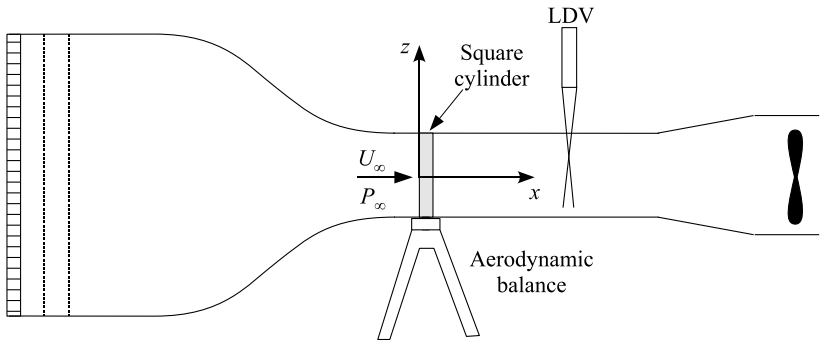

Fig. 2. Schematic diagram of the experimental set-up.

the control system with respect to the flow conditions. Finally, the efficiency of this system is assessed in Section 5 over a broad range of flow conditions.

2. Experimental set-up

2.1. The experimental facility

Experiments were performed in a subsonic open-loop wind tunnel with a 2 m long and 50 cm wide square test section (see Fig. 2). A very low residual turbulence level ($< 0.4\%$) was achieved by coupling a settling chamber equipped with honeycomb and screens to a (16:1) contraction located in front of the working section. The free-stream velocity U_∞ was inferred from the pressure drop measured in the contraction. The maximum flow velocity without obstacle was 60 m/s. As shown in Fig. 3, the roof of the working section was equipped with a movable glass window enabling velocity measurement via an optical technique (see below for more details).

Two aluminum cylinders with a square section were used in the framework of this study. One of these models was used as a reference, while the other was fitted with the control system introduced in the next section. The width H of the cylinders was equal to 60 mm and their front face was located around $8H$ downstream from the working section inlet. The cylinders almost spanned the channel resulting in a blockage ratio of 12% and an aspect ratio of 8.3. In this study, the Reynolds number $Re = U_\infty H/\nu$ (with ν the kinematic viscosity) was varied from 2×10^4 to 8×10^4. The origin of the coordinate system used in the following coincides with the center of the front face of the cylinder as displayed in Figs. 2 and 3. In the experiments described here the models were mounted so that the front face was normal to the direction of the upstream flow and that their axis was aligned with gravity (i.e. z-direction here).

2.2. The measurement techniques

The velocity field in the vicinity of the square cylinder was investigated by means of two-components (514.5 nm, 488 nm) Laser Doppler Velocimetry (LDV) system with a 6-W Argon-Ion laser (Spectra-Physics, Stabilite 2017) as light source. The flow seeding was ensured by saturating the wind tunnel room with olive oil droplets (~ 1 µm in diameter) generated by a particle seeding apparatus. The LDV probe was mounted on a 3D traversing system controlled by a computer and data were collected in the backward mode and processed with a BSA processor (Dantec) set in a non-coincident single measurement per burst mode. Velocity measurements were performed in the horizontal mid-plane (i.e. $z = 0$) of the working section. The constraints induced by the model geometry and the set-up configuration prevented us from probing the wall normal velocity closer than $0.3H$ from the cylinder surface, while the wall tangential velocity was probed up to $0.05H$ from this surface. The characteristic length scales of the measurement volume were 80 µm in x- and y-directions and 1 mm in z-direction. For each measurement point, several parameters such as the photomultiplier intensity and/or the window filtering were adjusted to optimize the mean data rate. Regarding the investigated region of the flow, the sampling rate was ranging from 2 kHz to 20 kHz resulting in time-series lasting between 50 s (close to the cylinder) and 5 s (in the free stream), respectively. These values were high enough to resolve the large scale flow dynamics. The LDA technique is known to produce non-equidistant time samples avoiding consequently a direct spectral analysis (Fourier transform). To overcome this drawback, a linear interpolation method was used to recover uniformly sampled data in order to investigate the large scale dynamics of the flow since this procedure only alters the high frequency range.

The global aerodynamics efforts acting on the square cylinder were obtained using a six internal components balance which was calibrated separately with masses covering the entire range of force measured in this study. The force signal was collected by means of a 12-bits data acquisition card with a sampling rate set at 10 Hz. For each measurement, the integration time was equal to 60 s. The time averaged force was then calculated by subtracting the residual force recorded with flow at rest over 30 s before and after each measurement point. The uncertainties were estimated to lie within the range 2% (highest Re) to 10% (lowest Re).

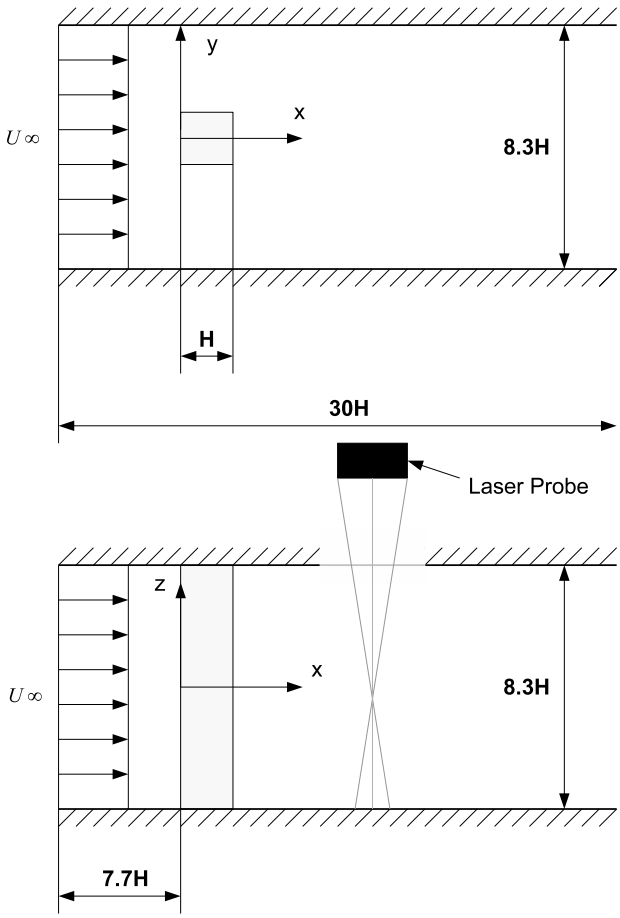

Fig. 3. Schematic diagram of the working section and the coordinate system.

Besides the force measurement, the pressure distribution around the square cylinder was investigated by means of 46 taps distributed in the mid-span of the model. Pressure taps were connected to a multiplexed pressure transducer (Scanivalve, CTRL2/S2-S6) through 1 m long tubing of 1.6 mm inner diameter. The pressure reference, P_∞, measured at the inlet of the working section was also connected to the pressure transducer such that the collected signal was the differential pressure $\Delta P = P - P_\infty$. To improve the signal to noise ratio, the pressure signal was amplified and then low-pass filtered before being stored via a 16-bits data acquisition card. The sampling rate and the integration time were set at 1 kHz and 30 s, respectively.

3. The natural or uncontrolled flow

This section is dedicated to the investigation of the flow around the square cylinder without the control system. In the following, this configuration is referred to as either the natural or the uncontrolled flow.

It is well known that the forces acting on bluff bodies are mainly dominated by pressure forces [22] unlike streamlined bodies for which viscous forces cannot be neglected. The pressure coefficient $Cp = \Delta P/(\rho U_\infty^2/2)$ is thus used as a relevant variable to quantify the local fluid force exerted on the square cylinder. The pressure distribution around the uncontrolled cylinder measured for $Re = 2 \times 10^4$ is displayed in Fig. 4. For sake of clarity, the faces of the square cylinder have been decomposed as follows:

i. the front face (AB);
ii. the base (CD);
iii. the sides (BC and DA).

It is worth noticing that the pressure distribution is symmetric with respect to the y-axis meaning that the mean lift is null. Consequently, we only focus on the half cylinder (i.e. $y \geqslant 0$) in the following.

As expected, the front face AB is featured by a strong pressure level where the maximum value $Cp = 1$ corresponds to the stagnation pressure. The sudden pressure drop observable at corner B results from the flow separation which induces

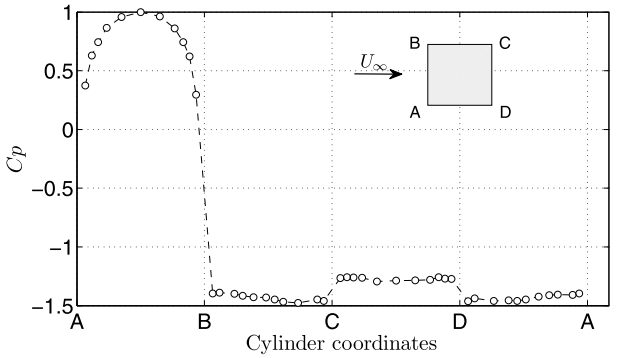

Fig. 4. Pressure coefficient distribution around the uncontrolled square cylinder ($Re = 2 \times 10^4$). The insert illustrates the notation used to describe the spatial location of the pressure taps around the cylinder.

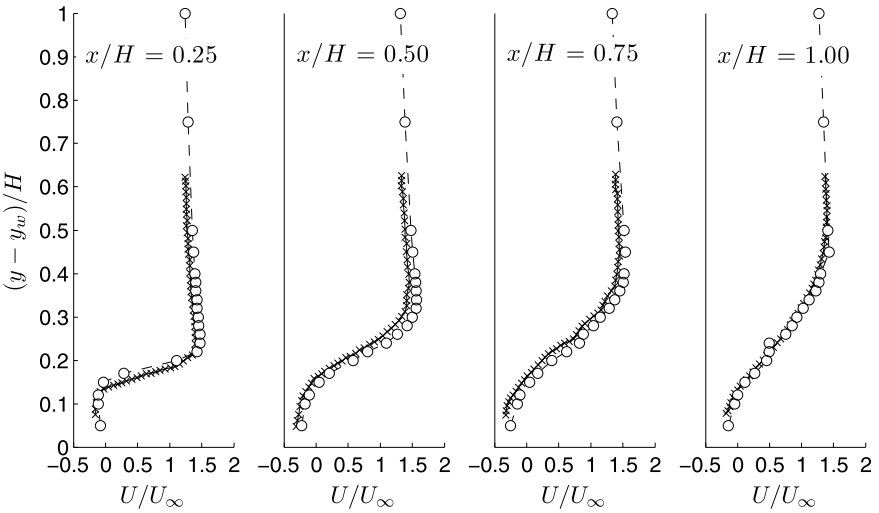

Fig. 5. Dimensionless streamwise mean velocity profiles U/U_∞ measured on the side BC at several distances downstream from the corner B ($Re = 2 \times 10^4$). The vertical axis represents the distance from the wall $y - y_w$ normalized by H. Our results (open circles) are compared to those reported by Lyn and Rodi [21] at similar Re (crosses).

the formation of a recirculation region on the side of the square cylinder. This is well supported by the profiles of the normalized streamwise mean velocity U/U_∞ plotted in Fig. 5 which exhibit a region close to the side wall (here BC) where the streamwise velocity is negative. Note that, for convenience, we introduce the wall location y_w so that $y - y_w$ represents the distance from the wall. Our results are in good agreement with those reported by Lyn and Rodi [21] which have been added in Fig. 5 for comparison.

The typical size of the recirculation region may be characterized by the location of the velocity bulge observable for the three first streamwise distances in Fig. 5. One can see that the recirculation region grows with increasing distance until $x/H = 0.75$ which coincides with the minimum pressure level (see Fig. 4). This specific position is representative of the location of the vortex core (V_1, hereafter) featuring the recirculation region bounded by the cylinder side as illustrated in Fig. 6.

The low pressure plateau on the base (CD) of the model reflects the presence of another recirculation region. It is important to note that the drag force is induced by the asymmetry of the pressure distribution between the front and the base faces. The near wake of the uncontrolled cylinder may be characterized by the points V_2 and S introduced in Fig. 6. The former represents the vortex core position of the base flow recirculation, while the latter stands for the location of the stagnation point delineating the recirculation region in the wake.

In addition to the mean flow topology, the dominant dynamics of the flow around the uncontrolled square cylinder has also been studied. The natural vortex shedding frequency of the flow, f_n, was determined using a spectral analysis of the velocity signal as illustrated in Fig. 7 for several Re. The related natural Strouhal number St_n ($\equiv f_n H/U_\infty$) remains almost constant ($St_n = 0.143 \pm 0.002$) over the range of Re used here. This value falls into the range reported in literature (see e.g. [23]).

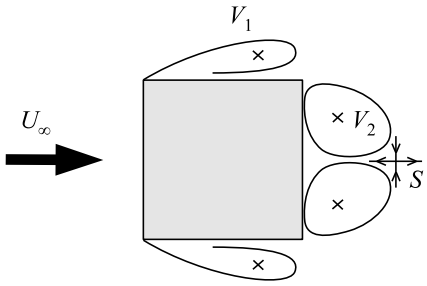

Fig. 6. Schematic of the flow topology in the vicinity of the uncontrolled square cylinder. The position V_1 stands for the average location of the vortex core of the recirculation regions on the side. The positions V_2 and S denote the average locations of the vortex core and the stagnation point characterizing the recirculation region on the base, respectively.

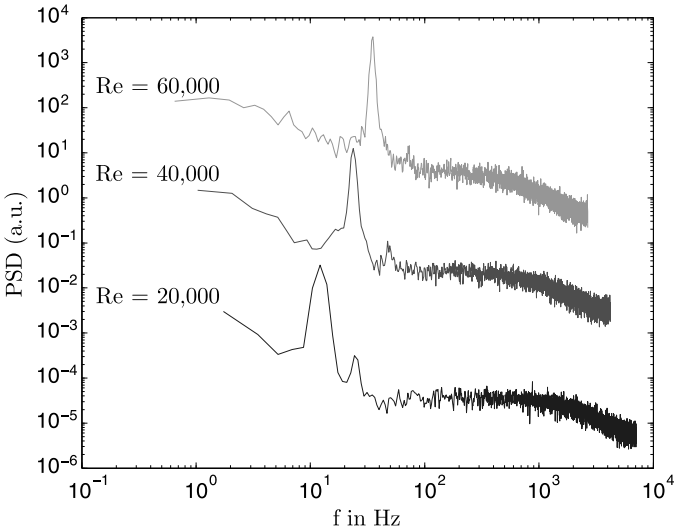

Fig. 7. Power spectra of velocity as functions of the frequency f computed in the near wake ($x/H = 2$, $y/H = 2.4$) of the uncontrolled square cylinder for several *Re*. For clarity, the curves have been shifted along the vertical axis.

4. The passive control system

4.1. The design

The control system investigated in this study which consists of a couple of flaps has been designed to mimic some features of bird's feathers. For that purpose, the flaps are built from the combination of a rigid frame and a porous fabric simulating the shaft and the vane, respectively. A schematic of the control flap is given in Fig. 8(a). Even though the control system developed in this study is inspired from bird's feathers, it is important to notice that we do not intend to reproduce them identically. The mechanisms implied in bird's flight may thus be significantly different from those observed here.

Besides the reference square cylinder, a similar model has been fitted with this original control system. Each flap is set on one side of the controlled square cylinder at a distance x_f downstream from the corners A or B. The flaps are fixed on the cylinder by means of tape so that they can freely rotate around their leading edge. An illustration of the experimental set-up of the control system is given in Fig. 8(b). In this study, the chord c and the thickness e of the flaps are equal to 35 mm and 2 mm, respectively. Their wingspan L is slightly smaller than the square cylinder span in order to prevent friction on the wind tunnel walls. Note that all experiments have been performed with the square cylinder axis aligned with the gravity and that the sides of the controlled square cylinder have been machined so that, when the fluid is at rest, the flaps fit into the walls.

According to the results reported in Section 3, when the fluid passes around the model, the side walls of the cylinder are subjected to a low pressure level inducing a suction effect which increases with increasing *Re*. Beyond a critical *Re*, the movable flaps depart from the cylinder surface and then flutter around a mean position. As no external power supply is required to activate our control system, the latter is referred to as a self-adaptive passive control device. The rigid frame which is made from solid ABS (rapid prototyping) has been designed to stiffen the flaps, preventing waviness during their motion. Meanwhile, in order to lighten the flap, the ratio of the area covered by its solid structure to the reference surface cL has been restricted to about 50% (see Fig. 8(a)). The porous fabric which is used to mimic the vane of the bird's feather

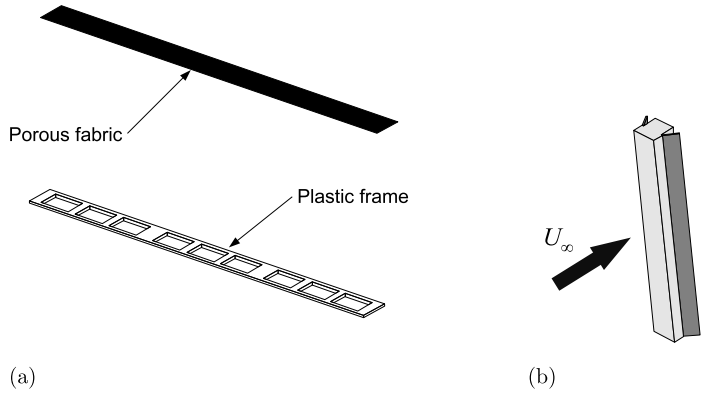

Fig. 8. (a) Exploded view of the self-adaptive control system made from the combination of a rigid frame (ABS plastic) and a porous fabric (silk). (b) Schematic of the controlled square cylinder.

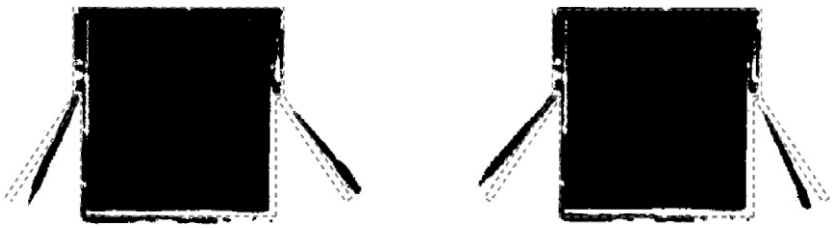

Fig. 9. Typical snapshots of the movable flaps ($Re = 6 \times 10^4$). The dashed contour symbolizes the average position of the flaps.

is made from a commercial silk covering the entire flap area cL. To avoid the propagation of spanwise waves, the fabric is glued onto the solid frame.

Note that even though three different positions of the fixation x_f have been tested, we only report the results obtained for $x_f = 25$ mm which has been found to be the most efficient. It is worth noticing that at this specific position, the center of the flaps roughly coincides with the location of the vortex core V_1 introduced in Fig. 6.

4.2. The flap dynamics

In order to understand the coupling between the flow and the control system, the dynamics of the movable flaps has been investigated. For that purpose, the time evolution of the position of the flaps has been evaluated on images recorded by means of a camera with a sampling rate of 300 frames per second. This sampling rate is at least 8 times larger than the highest vortex shedding frequency f_n observed for the natural flow (see Section 3).

The motion of both flaps is illustrated in Fig. 9 which shows two typical positions reached by the movable flaps for $Re = 6 \times 10^4$. For comparison, the average position of the flaps has been drawn (dashed contour). One can see that significant departures from the average position are achieved during the experiments. Note that for helping the comparison, a threshold procedure has been designed to convert the original images into binary images.

The dynamics of the movable flaps can be characterized by the time evolution of the angle $\theta_j(t)$ where the subscript j equals to either 1 or 2 depending on which flap is considered. A schematic of the geometrical representation is given in Fig. 10(a). Furthermore, we introduce the local coordinate system (x', y') related to the average position of the flaps, i.e. $\langle\theta_j\rangle$ (where $\langle\ \rangle$ stands for the time average), as shown in Fig. 10(b). In these diagrams, the points P_j represent the pivot around which the flaps rotate, while the points F_j denote the instantaneous position of the tip of the flaps.

A specific algorithm has been developed to recover the time-series $\theta_j(t)$ by evaluating the position of the flaps on each snapshot. The uncertainties associated with this procedure have been estimated to be lower than 2%. The instantaneous location of the points F_j in the local coordinate system (x', y') can therefore be defined as follows:

$$F_j(t) \equiv \begin{cases} x'_j(t) = c\sin\big(\theta_j(t) - \langle\theta_j\rangle\big) \\ y'_j(t) = c\cos\big(\theta_j(t) - \langle\theta_j\rangle\big) \end{cases} \tag{1}$$

The dimensionless trajectories of the points F_j calculated according to Eq. (1) for $Re = 2 \times 10^4$, $Re = 4 \times 10^4$ and $Re = 6 \times 10^4$ are plotted in Figs. 11(a), 11(c) and 11(e), respectively. These results indicate that the amplitude of the rotation around the equilibrium state, i.e. $\langle x'_j\rangle/H = 0$ and $\langle y'_j\rangle/H = c/H$, increases with increasing Re.

To emphasize this behavior, we introduce the fluctuating angle $\theta'_j(t) = \theta_j(t) - \langle\theta_j\rangle$. The deviation from the equilibrium state can therefore be quantified by the scatter plot of the normalized fluctuating angles $\theta'_j(t)/\langle\theta_j\rangle$ as displayed in Figs. 11(b),

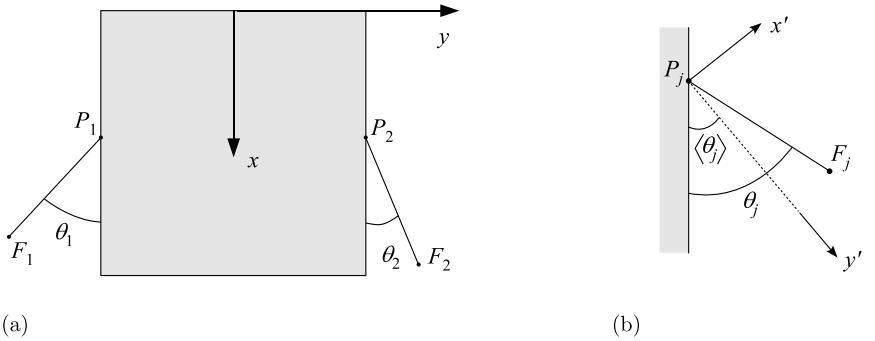

Fig. 10. (a) Schematic of the geometrical notation used to described the instantaneous position of the flaps. (b) Local coordinate system attached to the average position of a flap.

11(d) and 11(f) for $Re = 2 \times 10^4$, $Re = 4 \times 10^4$ and $Re = 6 \times 10^4$, respectively. For the lowest *Re*, the deviation from the equilibrium angle remains smaller than 10%, while it reaches up to 30% for the highest *Re*. Furthermore, these results highlight a noticeable modification in the shape of the scatter plots with respect to *Re*. The elongation of the scatter plot observable beyond $Re = 4 \times 10^4$ indicates that the motion of both flaps become dependent on each other. Indeed, the alignment of the scatter plots along the slope -1 (solid lines in Figs. 11(b), 11(d) and 11(f)) means that both flaps rotate in phase.

The dynamics of a single flap can be studied by means of the auto-correlation coefficient defined as follows:

$$R_{\theta_j\theta_j}(\tau) = \frac{\langle \theta'_j(t+\tau)\theta'_j(t)\rangle}{\langle \theta'_j(t)^2\rangle} \tag{2}$$

where τ is the time lag. The variation of $R_{\theta_1\theta_1}$ computed for several *Re* is plotted in Fig. 12(a). For sake of clarity, we do not report the variation of $R_{\theta_2\theta_2}$ since no significant difference with $R_{\theta_1\theta_1}$ has been observed. In order to highlight the differences with the natural (i.e. uncontrolled) flow, the time lag τ is normalized by the natural vortex shedding frequency f_n reported previously. The shape of $R_{\theta_1\theta_1}$ indicates that the rotating motion of the flaps is almost periodic for each *Re* used in this study. However, the dimensionless rotation frequency of the flaps f_r/f_n is clearly dependent on *Re*. Indeed, for the lowest *Re*, f_r is slightly higher than the natural vortex shedding frequency ($f_r \approx 1.2 f_n$), while it is smaller for the two largest *Re* ($f_r \approx 0.6 f_n$). We discuss further these results in the following subsection.

The relative motion of both flaps can be quantified by means of the cross-correlation coefficient:

$$R_{\theta_1\theta_2}(\tau) = \frac{\langle \theta'_1(t+\tau)\theta'_2(t)\rangle}{\sqrt{\langle \theta'_1(t)^2\rangle}\sqrt{\langle \theta'_2(t)^2\rangle}} \tag{3}$$

The variation of $R_{\theta_1\theta_2}$ displayed in Fig. 12(b) confirms that both flaps move with the same frequency f_r. However, at $\tau f_n = 0$, the cross-correlation coefficient is almost null for $Re = 2 \times 10^4$ meaning therefore that the flaps' motion is not synchronous. On the contrary, the high value of $R_{\theta_1\theta_2}$ observed at $\tau f_n = 0$ for $Re = 6 \times 10^4$, indicates that the flaps rotate in phase. Concerning the intermediate *Re*, i.e. $Re = 4 \times 10^4$, one can see a slight shift in time revealing that the relative flap rotation is not exactly synchronous.

4.3. The fluid–structure coupling

In order to compare the large scale flow dynamics with that of the movable flaps, we plot in Fig. 13 the power spectra of velocity measured in the near wake ($x/H = 2$, $y/H = 2.4$) of the controlled square cylinder. In this plot, the spectral frequency f is normalized by the natural vortex shedding frequency f_n. For the lowest *Re*, i.e. $Re = 2 \times 10^4$, the wake is dominated by a single frequency f_{ci} which is comparable to the rotation frequency f_r of the flaps as shown in the previous subsection. This frequency features the vortex shedding of the controlled flow. The related Strouhal number St_i ($\equiv f_{ci} H/U_\infty$) deviates noticeably from the natural one ($St_i = 0.175 \approx 1.2 St_n$) in agreement with usual observations reported in fluid/structure interactions (see e.g. [17]). For instance, studying the flow modification around a square cylinder oscillating in a stream, Bearman and Obajasu [24] revealed the occurrence of a lock-in regime between the vortex shedding and the cylinder oscillation. Such behavior was also reported by de Langre [25] who studied the linear stability of a circular cylinder subjected to vortex-induced vibrations.

For higher *Re*, the wake remains dominated by the vortex shedding characterized by $St_i = 0.175$ as evidenced in Fig. 13. However, another energetic mode arises at a lower frequency f_{cg}. This phenomenon coincides with the synchronization of the motion of both flaps (i.e. $f_{cg} = f_r$). One can notice that the ratio f_{ci}/f_{cg} increases with increasing *Re*. Meanwhile, the ratio of the energy contained in the high frequency mode (i.e. related to f_{ci}) to that contained in the low frequency mode (i.e. related to f_{cg}) decreases. This evolution may be interpreted as a modification of the wake pattern such as reported in

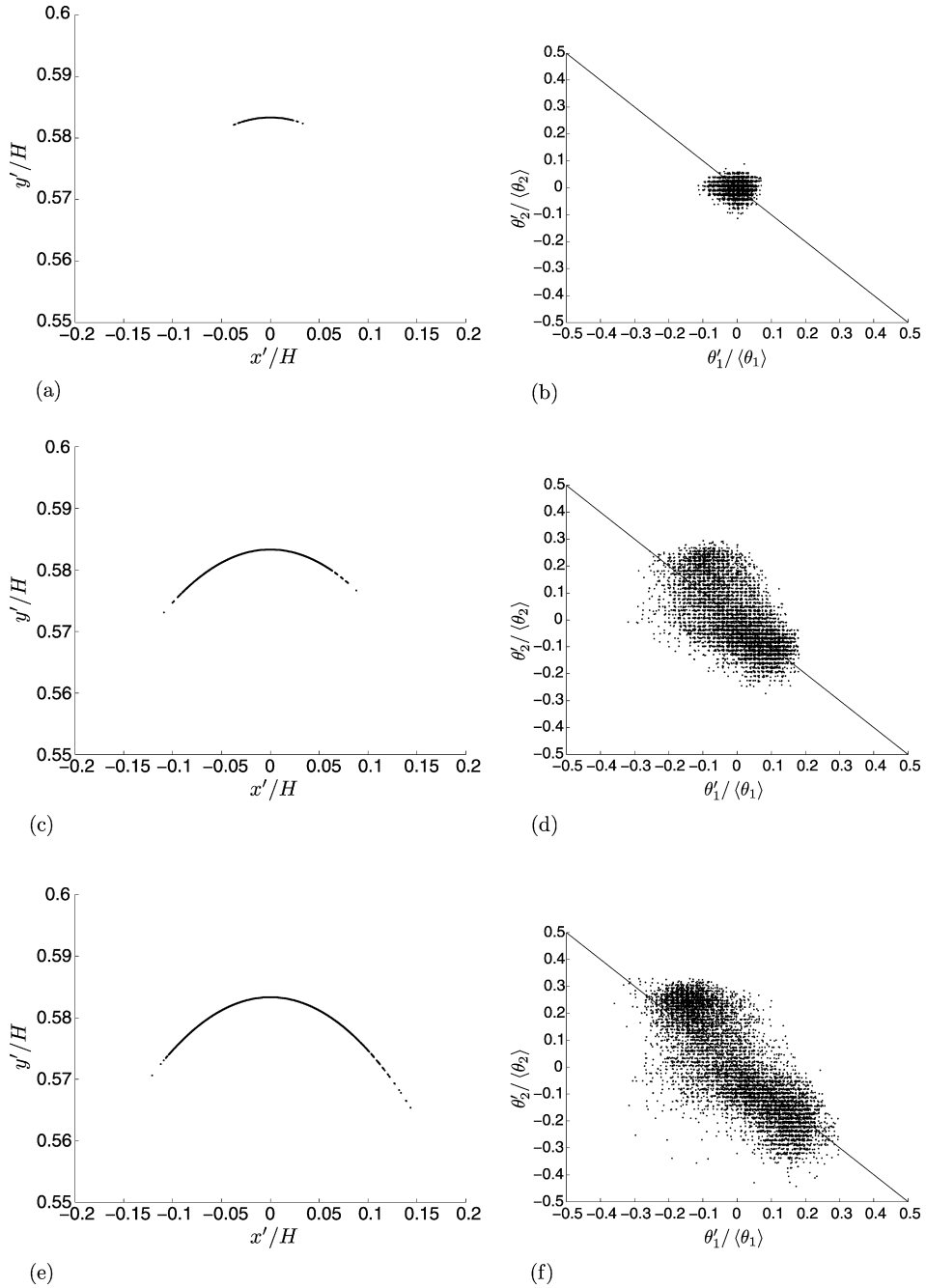

Fig. 11. Trajectories of the trailing edge of the movable flaps: (a) $Re = 2 \times 10^4$, (c) $Re = 4 \times 10^4$ and (e) $Re = 6 \times 10^4$. Scatter plot of the instantaneous angle of the movable flaps: (b) $Re = 2 \times 10^4$, (d) $Re = 4 \times 10^4$ and (f) $Re = 6 \times 10^4$. The straight line represents the curve $\theta_2'/\langle\theta_2\rangle = -\theta_1'/\langle\theta_1\rangle$.

vortex-induced vibration (see e.g. [26]) or in active flow control (see e.g. [27]). However, further experiments and analysis would be required so as to address properly this issue.

5. The controlled flow

This subsection is dedicated to the investigation of the flow controlled by the self-adaptive device. The velocity measurements and the pressure distribution around the square cylinder are analyzed to depict the mechanism of the interplay between the control system and the flow. Finally, the efficiency of the control system is evaluated by means of drag force measurement.

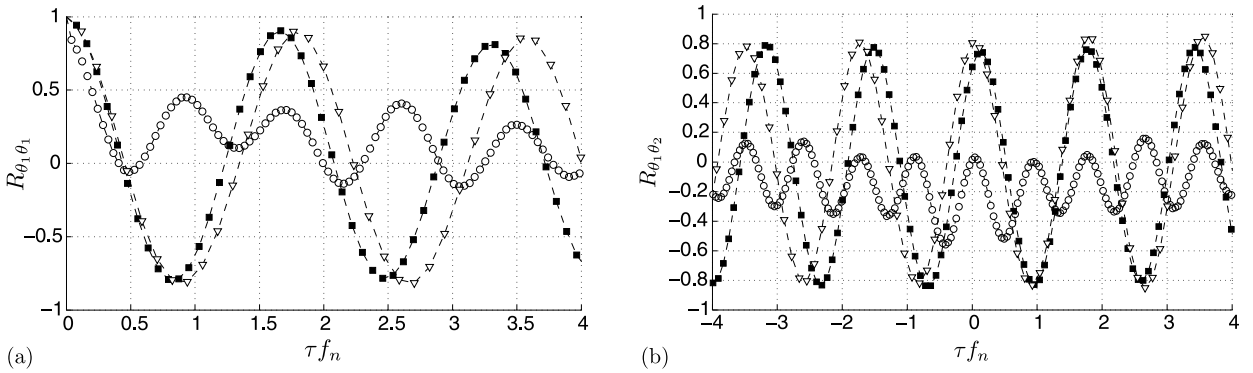

Fig. 12. Evolution of (a) $R_{\theta_1\theta_1}$ and (b) $R_{\theta_1\theta_2}$ vs. the dimensionless time lag τf_n for $Re = 2 \times 10^4$ (open circles), $Re = 4 \times 10^4$ (closed squares) and $Re = 6 \times 10^4$ (open triangles).

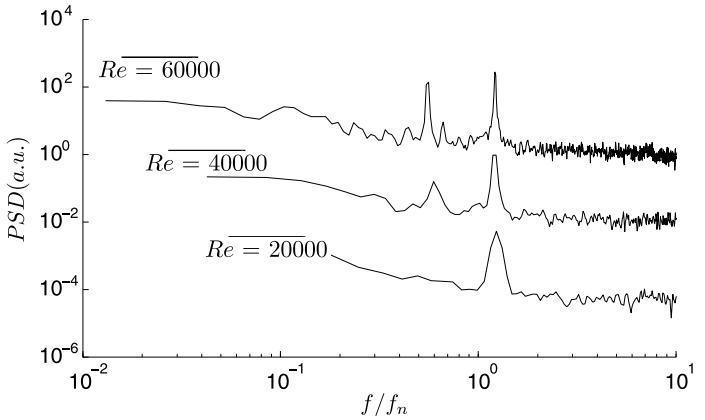

Fig. 13. Power spectra of velocity as a function of the normalized frequency f/f_n computed in the near wake ($x/H = 2$, $y/H = 2.4$) of the controlled square cylinder for several Reynolds numbers. For clarity, the curves have been shifted along the vertical axis.

5.1. The flow topology modification

Fig. 14(a) compares the velocity profiles U/U_∞ measured in both the uncontrolled and the controlled cases at $x/H = 0.25$ for $Re = 2 \times 10^4$. Note that for the controlled flow, the crossing of the laser beams and the flap trajectory restricts the investigation of the velocity field to $(y - y_w)/H \geqslant 0.17$.

Even though the shape of both curves are similar, one can clearly remark that the recirculation region is enlarged by the control system. However, beyond $(y - y_w)/H = 0.25$, both velocity profiles collapse meaning that the outer flow is almost unaffected by the presence of the movable flaps. This is an important result implying that the blockage of the flow is almost identical in both cases.

The modification of the near wake is evidenced in Fig. 14(b) which shows the velocity profile U/U_∞ measured for both the uncontrolled and the controlled square cylinders at $x/H = 2$ for $Re = 2 \times 10^4$. The velocity deficit observed in both cases is a feature of wakes. However, the spreading of the uncontrolled wake is larger than that of the controlled one. Moreover, one can see that, at this position, the controlled wake is characterized by a region ($y/H \leqslant 0.40$) where $U \leqslant 0$, unlike the uncontrolled wake. This implies that the location of the stagnation point S delineating the base recirculation region has moved farther downstream in the controlled case.

According to the results displayed in Figs. 14(a) and 14(b), we propose a simple representation of the mean topology of the controlled flow which is described in Fig. 15. In that representation, two recirculation regions are separated by the movable flaps. The vortex associated to V_1 is expected to be pushed upstream by the flap motion. Meanwhile, the pressure level downstream from the flaps (i.e. right-hand side in Fig. 15) is expected to increase due to the pressure drop induced by the fluid passing through the porous fabric. As a consequence, the vortex core V_2 of the second recirculation region, and accordingly the stagnation point S, are expected to move downstream their positions in the uncontrolled case. Even though this scenario is supported by measurements reported elsewhere [28], we stress that the mean flow topology depicted in Fig. 15 would require further investigations to be confirmed. This issue is beyond the scope of the present paper and is thus left for future studies.

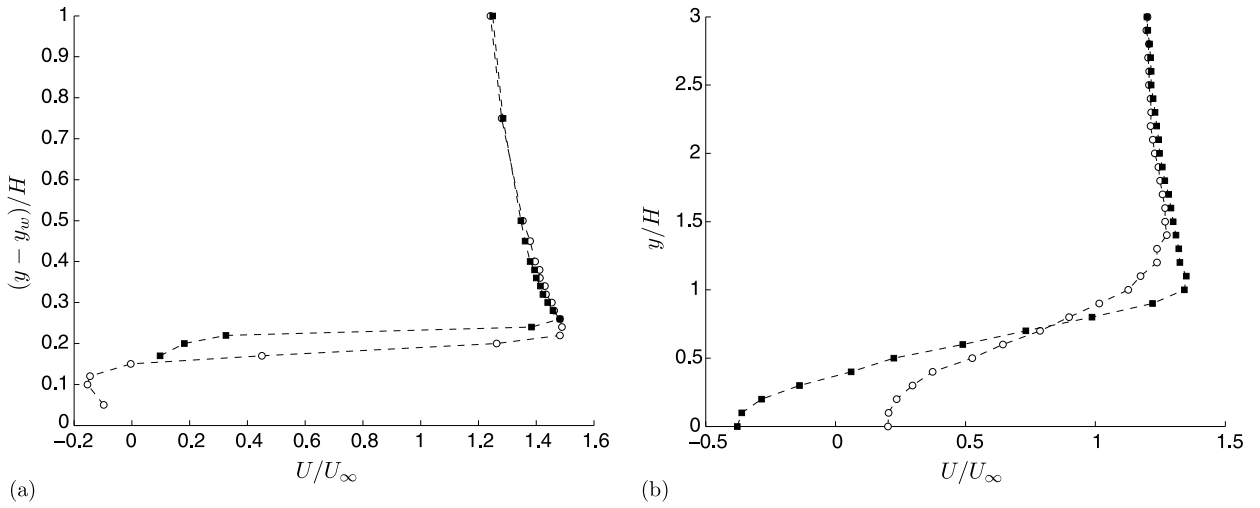

Fig. 14. Profiles of the dimensionless streamwise mean velocity U/U_∞ measured (a) on the side at $x/H = 0.25$ and (b) in the wake at $x/H = 2$ ($Re = 2 \times 10^4$). The results obtained for both the uncontrolled (open circles) and the controlled (closed squares) cylinders are compared.

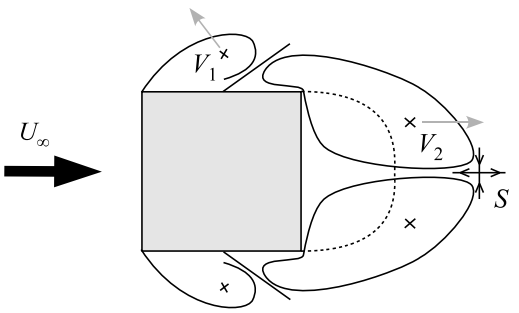

Fig. 15. Schematic of the flow around the square cylinder fitted with the self-adaptive movable flaps. The gray arrows symbolize the expected displacement of the vortex cores V_1 and V_2 relative to their natural position. The dashed line symbolizes the frontier of the recirculation region in the uncontrolled case.

5.2. The drag force reduction

The pressure distributions obtained in both the uncontrolled and the controlled flows are plotted in Figs. 16(a)–16(c) for several *Re*. One can see that, independently of *Re*, the control system significantly modifies the pressure distribution on the lateral sides (i.e. BC and DA) and the base (i.e. CD) as well, whereas the stagnation face (i.e. AB) is unaffected. The pressure jump δP visible on the both sides of the controlled cylinder coincides with the position of the leading edge of the movable flaps.

Assuming that each flap can be assimilated to a screen with a given blockage ratio and that δP is representative of the pressure drop across the flaps, it comes [29]

$$\delta P^\star = \frac{\delta P}{\frac{1}{2}\rho U_\infty^2} \sim G(Re) \tag{4}$$

where $\delta P^\star$ is the dimensionless pressure drop across the flaps and $G(Re)$ is a dimensionless function. The evolution of $\delta P^\star$ computed from the pressure distribution is plotted in Fig. 17 with respect to *Re*.

This plot emphasizes that the normalized pressure drop $\delta P^\star$ decreases with increasing *Re* in agreement with the results reported by Groth and Johansson [30]. In the present study, the fitting (in the least-mean square sense) of our experimental data yields

$$\delta P^\star = K Re^{-\gamma} \tag{5}$$

where $K \approx 32$ and $\gamma \approx 0.4$, at least for the range of *Re* tested here. According to this result, the pressure drop δP evolves like $Re^{1.6}$. However, one can notice that the pressure upstream from the flap (left-hand side in Fig. 15) remains almost constant with respect to *Re*. This confirms that the pressure downstream from the flap (right-hand side in Fig. 15) increases with increasing *Re*. However, we stress that care should be taken in extrapolating this trend to higher *Re*. More data are required for a conclusive assessment of this issue which is therefore left for future studies.

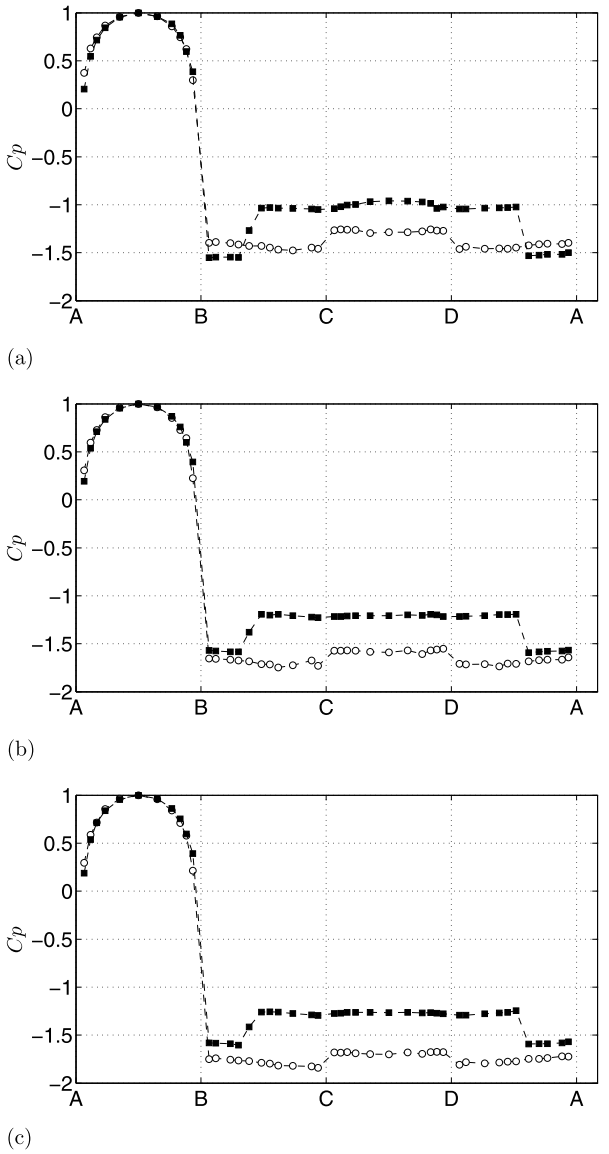

Fig. 16. Pressure distribution around both the uncontrolled (open circles) and the controlled (closed squares) square cylinders obtained for (a) $Re = 2 \times 10^4$, (b) $Re = 4 \times 10^4$ and (c) $Re = 6 \times 10^4$.

The main consequence of the increase of the base pressure in the controlled case is the reduction of the drag force. In order to evaluate the efficiency of the control system, the drag coefficient C_D ($\equiv \frac{D}{\rho U_\infty^2 HL/2}$ with D the drag force) has been measured by means of a static load balance in both the uncontrolled and the controlled configurations. Fig. 18(a) shows the evolution of C_D as a function of Re. It is worth noticing that the values reported here are not corrected for the blockage effect (see e.g. [31]). However, we have checked that the differences between the uncontrolled and the controlled cases are not affected by these corrections. This can be explained by the fact that the control system does not change the blockage ratio as evidenced by the velocity profiles shown hereinbefore.

The self-adaptive control system improves significantly the aerodynamics of the square cylinder. Indeed, the drag reduction ranges from 17% to 25% over the entire range of Re used in this study (see Fig. 18(b)). These values are comparable to those reported by Shao and Wei [5] for similar Re. Furthermore, these results confirm that the control seems more efficient with increasing Re.

6. Conclusions

An original passive control system consisting of a couple of porous flaps has been developed and fitted on a square cylinder so that the flaps can freely rotate around their leading edge. These flaps have been designed to mimic the main

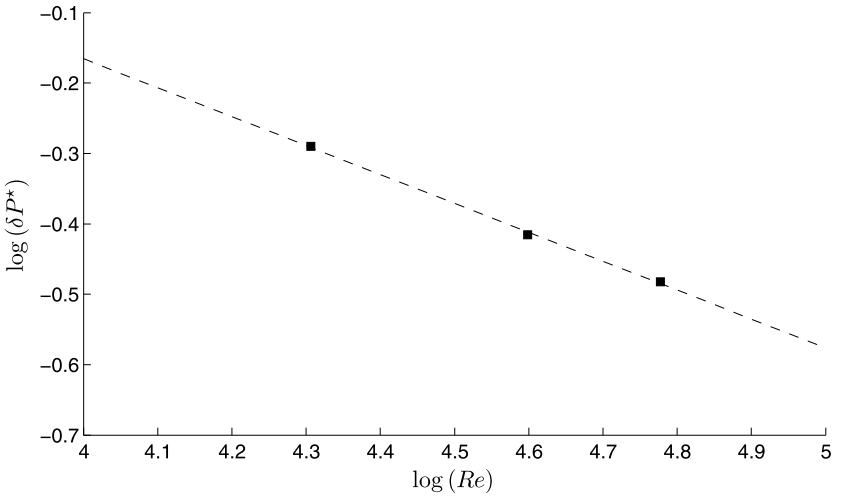

Fig. 17. Normalized pressure drop across the movable flaps as a function of *Re* in log–log representation. The dashed line symbolizes the curve $\delta P^{\star} = KRe^{-\gamma}$ with $K \approx 32$ and $\gamma \approx 0.4$.

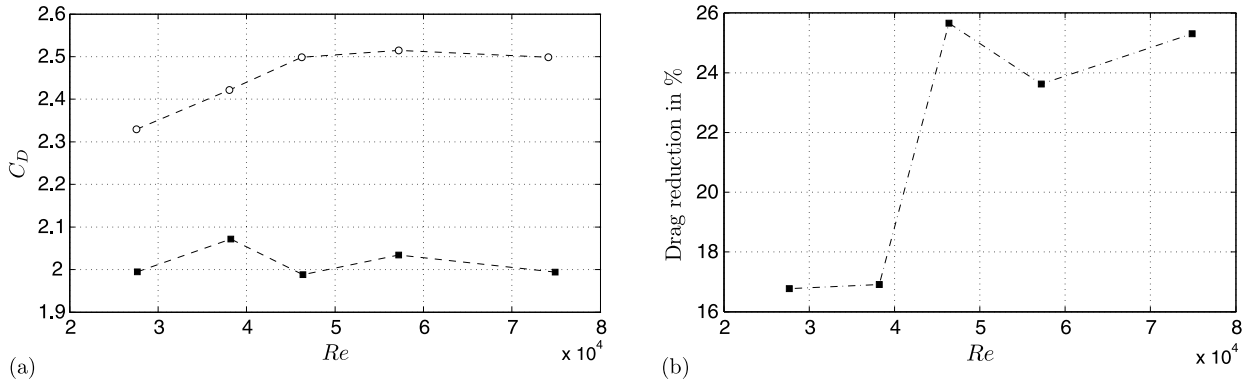

Fig. 18. (a) Drag coefficient as a function of the Reynolds number measured for the uncontrolled square cylinder (open circles) and for the controlled square cylinder (close squares). (b) Variation of the drag reduction against Reynolds number.

features of bird's feathers, i.e. the stiffness of the shaft coupled with the porosity of the vane. This goal has been achieved by assembling a rigid and light plastic skeleton with a porous fabric.

The device developed here can be assimilated to a self-adaptive passive control system which is activated by the reverse flow arising from the upstream corners of the square cylinder. For high enough Reynolds number, the flaps depart from the cylinder walls and flutter around a mean position. It has been shown that the amplitude of the flap motion increases with increasing Reynolds number. For low Reynolds number the rotation frequency of both flaps is slightly higher than that of the natural vortex shedding even though their motion seems asynchronous. On the other hand, the investigation of the relative motion of both flaps has revealed that for high enough Reynolds number the flaps rotate in phase at a frequency almost twice as small as the natural vortex shedding frequency. The spectral analysis performed in the near wake of the cylinder has exhibited a lock-in coupling between the flow and the movable flaps.

The efficiency of the control system has been evaluated by investigating the drag force. Comparing both the uncontrolled and the controlled cases, about 22% drag reduction has been obtained, in average, over the entire range of Reynolds numbers tested here. This enhancement of the aerodynamic performances is related to the increase of the base pressure in the controlled case. A simple mechanism accounting for this phenomenon has been suggested. In this scenario, the pressure drop across the porous fabric induces an increase of the pressure downstream the flaps. As a consequence, the vortex core of the recirculation region in the wake is expected to move downstream resulting in the increase of the base pressure. This scenario is supported by the evolution of the mean velocity reported in the wake.

Even though the results presented in this study are encouraging, further works are required to get a better understanding of the control system and the flow. For that purpose, the influence of relevant parameters such as the fabric porosity, for instance, will be investigated in future.

Acknowledgements

The authors are grateful to Mr. S. Loyer for his assistance during the experiments.

References

[1] M. Gad-el Hak, Flow Control: Passive, Active and Reactive Flow Management, Cambridge University Press, London, 2000.
[2] H. Choi, W.P. Jeon, J. Kim, Control of flow over a bluff body, Ann. Rev. Fluid Mech. 40 (2008) 113–139.
[3] P.W. Bearman, J.C. Owen, Reduction of bluff-body drag and suppression of vortex shedding by the introduction of wavy separation lines, J. Fluids Struct. 12 (1998) 123–130.
[4] J.C. Owen, P.W. Bearman, A.A. Szewczyk, Passive control of VIV with drag reduction, J. Fluids Struct. 15 (2001) 597–605.
[5] C.P. Shao, Q.D. Wei, Control of vortex shedding from a square cylinder, AIAA J. 46 (2008) 397–407.
[6] C.H. Bruneau, I. Mortazavi, Passive control of the flow around a square cylinder using porous media, Int. J. Numer. Meth. Fluids 46 (2004) 415–433.
[7] E. Stanewsky, Adaptive wing and flow control technology, Prog. Aerosp. Sci. 37 (2001) 583–667.
[8] M.H. Dickinson, F.O. Lehmann, S.P. Sane, Wing rotation and the aerodynamic basis of insect flight, Science 284 (1999) 1954–1960.
[9] R. Vepa, Biomimetic flight and flow control: learning from the birds, in: IUTAM Symposium on Flow Control and MEMS, 2008, pp. 443–447.
[10] G.K. Taylor, R.L. Nudds, A.L.R. Thomas, Flying and swimming animals cruise at Strouhal number tuned for high power efficiency, Nature 425 (2003) 707–711.
[11] M.S. Triantafyllou, G.S. Triantafyllou, R. Gopalkrishnan, Wake mechanics for thrust generation in oscillating foils, Phys. Fluids A 3 (1991) 2835–2837.
[12] F.P. Gosselin, E. de Langre, B.A. Machado-Almeida, Drag reduction of flexible plates by reconfiguration, J. Fluid Mech. 650 (2010) 319–341.
[13] F.E. Fish, G.V. Lauder, Passive and active flow control by swimming fishes and mammals, Ann. Rev. Fluid Mech. 38 (2006) 193–224, 247–266.
[14] D.W. Bechert, M. Bruse, W. Hage, R. Meyer, Fluid mechanics of biological surfaces and their technological application, Naturwissenchaften 87 (2000) 157–171.
[15] M.S. Triantafyllou, A.H. Techet, F.S. Hover, Review of experimental work in biomimetic foils, IEEE J. Oceanic Eng. 29 (2004) 585–594.
[16] S. Alben, M. Shelley, J. Zhang, Drag reduction through self-similar bending of a flexible body, Nature 420 (2002) 479–481.
[17] J. Favier, A. Dauptain, A. Basso, A. Bottaro, Passive separation control using a self-adaptive hairy coating, J. Fluid Mech. 627 (2009) 451–483.
[18] F.P. Gosselin, E. de Langre, Drag reduction by reconfiguration of a poroelastic system, J. Fluids Struct. 27 (2011) 1111–1123.
[19] W. Liebe, Der Auftrieb am Tragfügel: Entstehung und Zusammenbruch, Aerokurier 12 (1979) 1520–1523.
[20] M. Schatz, T. Knacke, F. Thiele, R. Meyer, W. Hage, D.W. Bechert, Separation control by self-activated movable flaps, AIAA Paper 1243-2004, Reno, 2004.
[21] D.A. Lyn, W. Rodi, The flapping shear layer formed by flow separation from the forward corner of a square cylinder, J. Fluid Mech. 261 (1994) 353–376.
[22] A. Roshko, On the wake and drag of bluff bodies, J. Aerosp. Sci. 22 (1955) 124–132.
[23] C. Norberg, Flow around rectangular cylinders: pressure forces and wake frequencies, J. Wind Eng. Ind. Aero. 49 (1993) 187–196.
[24] P.W. Bearman, E.D. Obasaju, An experimental study of pressure fluctuations on fixed and oscillating square-section cylinders, J. Fluid Mech. 119 (1982) 297–321.
[25] E. de Langre, Frequency lock-in is caused by coupled-mode flutter, J. Fluids Struct. 22 (2006) 783–791.
[26] T.L. Morse, C.H.K. Williamson, Prediction of vortex-induced vibration response by employing controlled motion, J. Fluid Mech. 634 (2009) 5–39.
[27] M. Pastoor, L. Henning, B.R. Noack, R. King, G. Tadmor, Feedback shear layer control for bluff body drag reduction, J. Fluid Mech. 608 (2008) 161–196.
[28] N. Mazellier, A. Kourta, Amélioration des performances aérodynamiques d'un profil au moyen d'un actionneur passif auto-adaptatif, in: Proceedings of the 20th Congrès Français de Mécanique, Besançon, France, 2011.
[29] E.M. Laws, J.L. Livesey, Flow through screens, Ann. Rev. Fluid Mech. 10 (1978) 247–266.
[30] J. Groth, A.V. Johansson, Turbulence reduction by screens, J. Fluid Mech. 197 (1988) 139–155.
[31] E.C. Maskell, A theory of the blockage effects on bluff bodies and stalled wings in a closed wind tunnel, R.A.E. Aero. Rep. No. 2685, 1963.